Nano Research
2023, 16(2): 2519–2527

ISSN 1998-0124 CN 11-5974/O4
https://doi.org/10.1007/s12274-022-5059-y

Research Article

WC/Co_7Fe_3 heterojunction embedded in N,P co-doped hierarchical carbon enables rechargeable/flexible Zn-air battery

Huimin Mao[1,2], Xiaobin Liu[1,2,4] (✉), Siqi Wu[1,2], Yixin Fu[1,2], Guishan Liu[1,2], Guizhong Zhou[1,2] (✉), and Lei Wang[1,2,3] (✉)

[1] *Key Laboratory of Eco-chemical Engineering, International Science and Technology Cooperation Base of Eco-chemical Engineering and Green Manufacturing, Qingdao University of Science and Technology, Qingdao 266042, China*
[2] *College of Environment and Safety Engineering, Qingdao University of Science and Technology, Qingdao 266042, China*
[3] *College of Chemistry and Molecular Engineering, Qingdao University of Science and Technology, Qingdao 266042, China*
[4] *Chaofeng Steel Structure Group Co., Ltd., Hangzhou 311215, China*

Received: 6 August 2022 / **Revised:** 13 September 2022 / **Accepted:** 14 September 2022

ABSTRACT

Rational design and synthesis of bifunctional oxygen electrocatalysts with high activity and stability are key challenges in the development of rechargeable Zn-air batteries (ZABs). In this paper, tungsten carbide (WC) and Co_7Fe_3 embedded in N,P co-doped hierarchical carbon (WC/Co_7Fe_3-NPHC) was prepared by using zeolite imidazolate frameworks as precursor. Density functional theory demonstrates that the mutual adjustment among the WC, Co_7Fe_3, and N,P co-doped carbon at the three-phase heterojunction interface makes the catalyst possess moderate adsorption strength, and greatly improves the conductivity and electron transfer rate of the catalyst. As a result, the WC/Co_7Fe_3-NPHC exhibits a low overall oxygen redox potential difference of 0.72 V, while the ZAB assembled by WC/Co_7Fe_3-NPHC as an air cathode exhibits ultra-long cycle stability of over 550 h. Futhermore, WC/Co_7Fe_3-NPHC can keep good charge and discharge stability at different bending angles when applied to flexible solid ZAB.

KEYWORDS

heterojunction, hierarchical structure, bifunctional oxygen electrocatalyst, Zn-air battery

1 Introduction

To solve the pressing problem of fossil fuels consumption and the consequent environmental pollution, great efforts have been made to develop clean and sustainable energy [1–3]. In terms of electrochemical energy, Zn-air batteries (ZABs) have high theoretical energy density of 1,086 $Wh{\cdot}kg^{-1}$ and low hazard liquid electrolytes, which are environmentally friendly, resource-rich, low-cost, and high safety, and are considered to be one of the most outstanding alternative technologies to meet future energy needs [4–7]. Oxygen evolution reaction (OER) and oxygen reduction reaction (ORR) are the core reactions of ZAB, which realize the reciprocal conversion of electric and chemical power [8, 9]. Despite the high cost and scarcity, Pt and Ir/RuO_2 are the most advanced ORR and OER electrocatalysts, respectively [10–13]. In addition, single function noble-based electrocatalyst makes the cathode must be loaded with two types of ORR/OER catalysts, thus reducing the payload of each catalyst and increasing the complexity of cell device manufacturing [14–17]. Therefore, the development of high efficiency and durable noble metal free difunctional electrocatalyst is the key to the practical application of ZAB [18, 19].

The construction of heterojunction interfaces is an effective strategy to improve the bifunctional oxygen electrocatalysis performance [20–22]. Tungsten carbide (WC) possesses a Pt-like d-band electron structure, which is easy to adsorb oxygen and owns great potential to promote ORR [23, 24]. Meanwhile, the CoFe-based metal alloy has different redox potentials and a large number of defects, exhibiting excellent OER electrocatalytic activity [25, 26]. Furthermore, the oxygen electrocatalysis activity of WC and CoFe-based metal could be enhanced by incorporated with heteroatom-doped carbon [27–30]. For example, Wang et al. successfully synthesized WC/N-doped carbon hybrids with unique bionic nodular structure, which showed good activity and robustness to ORR in alkaline solution [31]. Zhou et al. proposed a highly efficient synthesis method for the preparation of Fe_3Co_7@PCNSs heterostructured oxygen electrode materials, which provide rich active sites for the electrocatalytic activity of OER [32]. Therefore, effective construction of WC, Co_7Fe_3, and heteroatom-doped carbon heterostructure may simultaneously enhance the bifunctional oxygen electrocatalysis performance. Apart from the construction of heterojunction interfaces, building a hierarchical structure can increase the exposure of its active sites, effectively avoid the agglomeration of the catalyst, and provide a faster electron conduction path [33, 34]. For instance, Feng et al. demonstrated a new template-free approach to constructing three-dimensional (3D) carbon superstructures with ultra-high specific surface area, layered porous structure, and uniformly distributed electroactive sites [35]. Shao et al. synthesized a multistage carbon microtube@nanotube (CMT@CNT) core–shell structure, which

Address correspondence to Xiaobin Liu, liuxb@qust.edu.cn; Guizhong Zhou, zhougz@126.com; Lei Wang, inorchemwl@126.com

has a large electrochemical active surface area and abundant transport channels, and can guarantee the active site to participate in the reaction effectively even under high loading conditions [36].

Inspired by the above strategies, WC and Co_7Fe_3 embedded into N,P co-doped hierarchical carbon (WC/Co_7Fe_3-NPHC) was designed and synthesized for the first time by using zeolitic imidazolate frameworks (ZIFs) as precursors [37, 38]. Profiting from the synergistic effect among the WC, Co_7Fe_3, and N,P co-doped carbon at the three-phase heterojunction interface, as well as the distinct hierarchical carbon structure, the as-prepared WC/Co_7Fe_3-NPHC catalyst displays exceptional OER and ORR activities, with an overall oxygen redox potential difference of 0.72 V, which exceeded Pt/C+RuO_2 (0.74 V) and most of the reported non-noble metal catalysts within alkaline media. As an air cathode in ZAB, it reveals a superior peak power density of 270 mW·cm^{-2} and discharge voltage gap of 0.72 V, as well as ultra-high stability of 550 h at a current density of 10 mA·cm^{-2}, all of which are superior to the performance of Pt/C+RuO_2-based ZAB. According to the theoretical calculation, due to the mutual adjustment between the N,P co-doped carbon and Co_7Fe_3 and WC, the catalyst has moderate adsorption intensity, and greatly improves the conductivity and electron transfer rate of the material. This study expands the heterogeneous library of hierarchical materials and opens a new avenue for the development of low-cost and efficient dual-function catalysts, which is expected to replace the extensive use of precious metals in electrochemical energy systems.

2 Results and discussion

2.1 Preparation and characterization

The schematic process for the preparation of WC/Co_7Fe_3-NPHC is displayed in Fig. 1(a) [39, 40]. First of all, the hexagram P,W-ZnCoFe-ZIF precursor was obtained through a handy chemical precipitation process. The scanning electron microscopy (SEM) images in Fig. 1(b) illustrate the P,W-ZnCoFe-ZIF has a hexagram nanostructure, and the precursors with various amount of sodium phosphotungstate also produce such morphology (Figs. S1(a)–S1(c) in the Electronic Supplementary Material (ESM)), which indicates that in the presence of 2-methylimidazole, Zn^{2+}, Co^{2+}, and Fe^{2+} interact to form a heterogeneous ZIF-67 metal-organic frameworks, while phosphotungstic acid has little effect on the formation of hexagram-like morphology. Subsequently, the as-prepared ZnCoFe-ZIF was pyrolyzed at 900 °C under Ar atmosphere to obtain WC/Co_7Fe_3-NPHC catalyst that still maintains the hexagram structure, and a large amount carbon nanotubes are *in-situ* formed on the surface of the hexagram (Fig. 1(c)). The Co_7Fe_3 and WC heterojunctions are formed with the P,W-ZnCoFe-ZIF as self-sacrificing template, while the P source and dimethylimidazole are *in-situ* converted to N and P co-doped carbon. In addition, comparison samples with different amount of sodium phosphotungstic acid and different pyrolysis temperatures were also prepared. As shown in Figs. S1(d)–S1(f) in the ESM, the addition of different amount of sodium phosphotungstic acid

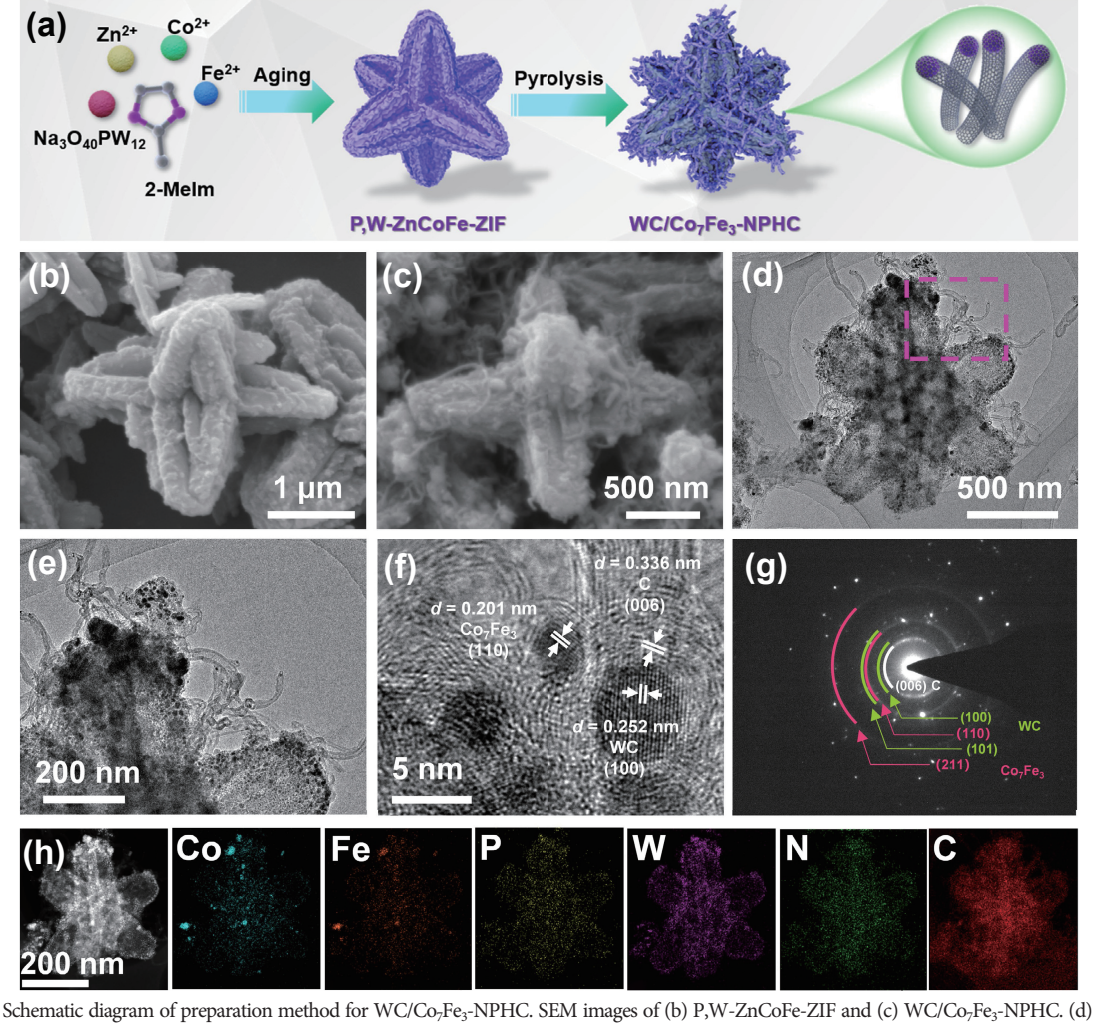

Figure 1 (a) Schematic diagram of preparation method for WC/Co_7Fe_3-NPHC. SEM images of (b) P,W-ZnCoFe-ZIF and (c) WC/Co_7Fe_3-NPHC. (d) and (e) TEM, (f) HR-TEM, (g) SAED, and (h) high-angle annular dark-field scanning transmission electron microscopy (HAADF-STEM) and elemental mapping images of WC/Co_7Fe_3-NPHC.

precursor can all lead to the formation of carbon nanotubes. By comparing the pyrolysis products of P,W-ZnCoFe-ZIF at different temperatures (Figs. S2(a) and S2(b) in the ESM), it can be found that there are more carbon nanotubes formed at 900 and 1,000 °C than at 800 °C, because the pores formed during the evaporation of Zn can further promote the generation of nanotubes in the sublimation process of carbon source at high temperature.

Figure 1(d) shows that the as-prepared P,W-ZnCoFe-ZIF displays hexagram-like structure with a lot of nanotubes embedded on the surface of hexagram, which is consistent with the SEM image. As shown in Fig. 1(e), the transmission electron microscopy (TEM) image indicates that a large number of ultrafine nanoparticles are embedded in the 3D hexagram carbon matrix and at the top of the one-dimensional (1D) carbon nanotubes. The formation of nanotubes can enhance the conductivity of catalyst and the apex structure can serve as a complementary active site for complex electrochemical reactions [41]. Furthermore, the high-resolution TEM (HR-TEM) image exhibits clear-defined lattice fringes with *d*-spacings of 0.201 and 0.252 nm, matching the (110) planes of the Co_7Fe_3 and (100) planes of WC, respectively, which are encapsulated by highly graphitic carbon shell (Fig. 1(f)). Additionally, the polycrystalline nature of CoFe is further demonstrated by selected area electron diffraction (SAED) images (Fig. 1(g)), where the diffraction rings correspond to the crystallographic planes of C, Co_7Fe_3, and WC, respectively. Moreover, the element mapping images confirm the uniform distribution of Co, Fe, P, W, N, and C element throughout the WC/Co_7Fe_3-NPHC (Fig. 1(h)).

The X-ray diffraction (XRD) analysis in Fig. 2(a) demonstrates the co-existence of WC and Co_7Fe_3 in WC/Co_7Fe_3-NPHC, where diffraction peaks at about 31.5°, 35.6°, and 48.3° are separately assigned to the (001), (100), and (101) planes of WC heterojunction (JCPDS No. 51-0939), and the peak at about 45.2° is assigned to the (110) plane of Co_7Fe_3 heterojunction (JCPDS No. 50-0795), further confirming the crystal structure of WC/Co_7Fe_3-NPHC catalyst. The XRD spectra of Co-Fe/NC were dominated by the Co phase and no characteristic peaks of Fe appeared, indicating that the Fe atoms are doped in the samples (Fig. S3 in the ESM). In addition, we further identified the carbon composition of WC/Co_7Fe_3-NPHC at different annealing temperatures by Raman spectroscopy. As shown in Fig. S4 in the ESM, significant peaks of disordered carbon (D band) and graphite layer (G band) appear at 1,350 and 1,585 cm^{-1}, respectively. The D band based on sp^3 bonding is caused by the lattice distortion of carbon and represents the defects contained in carbon, while the G band is related to the graphitization degree of sp^2 graphite carbon bond. The I_D/I_G of WC/Co_7Fe_3-NPHC series samples are all larger than 1, indicating that the material is rich in defects, and the I_D/I_G also decreases with the increase of annealing temperature. The smaller the I_D/I_G is, the higher the graphitization degree of the material is, indicating that the higher temperature is conducive to improving the graphitization degree of the material and thus improving the electrical conductivity. Therefore, selecting appropriate pyrolysis temperature can make the material have high graphitization degree and defect site at the same time, which is hopeful for promoting the electrical conductivity and catalytic activity. The porosity and specific surface area of the catalysts were investigated by N_2 adsorption–desorption measurement. The typical N_2 sorption curves of WC/Co_7Fe_3-NPHC (Fig. 2(b)) would be ascribed to Type IV isotherms, and the P/P_0 ratio of WC/Co_7Fe_3-NPHC shows an obvious hysteresis loop in the range of 0.8–1.0, manifesting the presence of rich mesoporous [42]. The Brunauer–Emmett–Teller (BET) surface area of WC/Co_7Fe_3-NPHC is up to 315.4 $m^2 \cdot g^{-1}$, which is conducive to exposing more

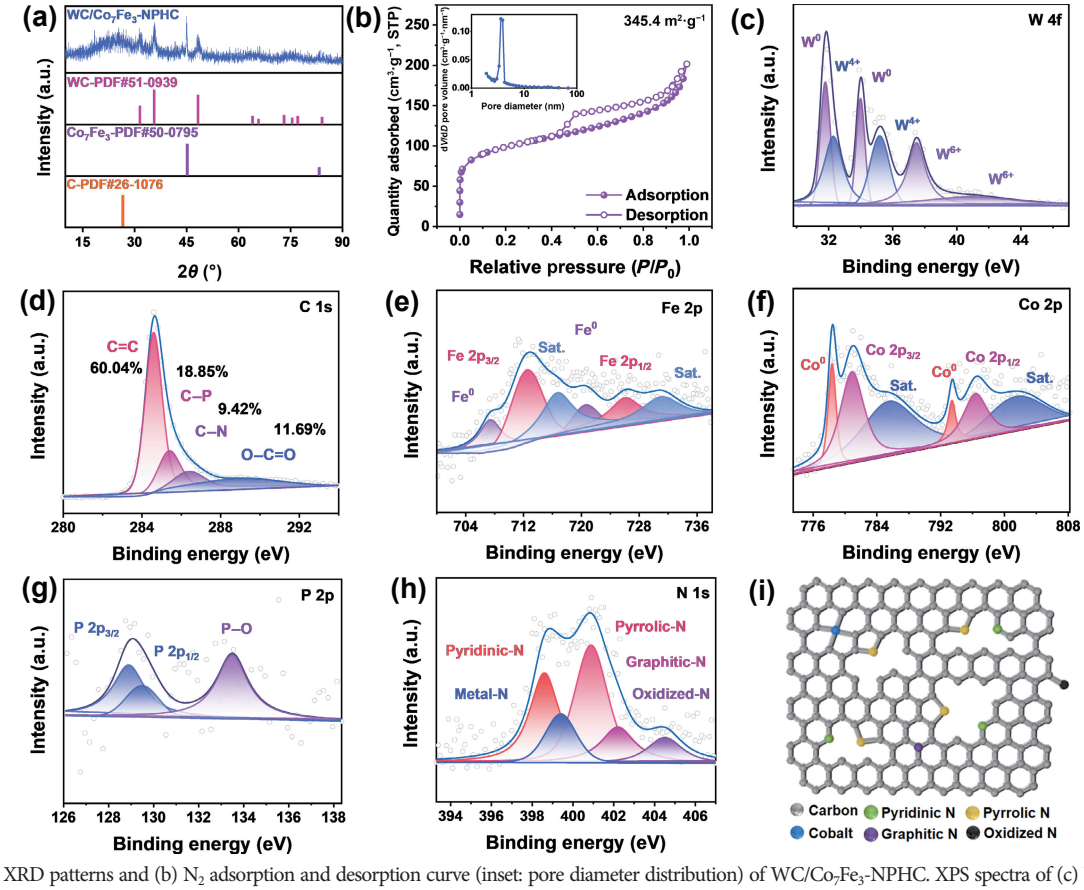

Figure 2 (a) XRD patterns and (b) N_2 adsorption and desorption curve (inset: pore diameter distribution) of WC/Co_7Fe_3-NPHC. XPS spectra of (c) W 4f peaks, (d) C 1s peaks, (e) Fe 2p peaks, (f) Co 2p peaks, (g) P 2p peaks, and (h) N 1s peaks of WC/Co_7Fe_3-NPHC. (i) Diagrammatic figure of nitrogen configuration of WC/Co_7Fe_3-NPHC.

active sites. The pore size distribution demonstrates that the particle size of materials is mostly about 4.0 nm mesoporous, which is beneficial for the diffusion of electrolyte and the utilization of active sites.

The surface elemental composition and chemical states of WC/Co_7Fe_3-NPHC were analyzed by X-ray photoelectron spectroscopy (XPS). The survey scan spectrum (Fig. S5 in the ESM) indicates the co-presence of Co, Fe, W, N, P, and C elements in the as-prepared WC/Co_7Fe_3-NPHC. The related XPS spectrum of W 4f is highly asymmetric, and can be deconvoluted into three sets of spin-orbital doublets. In the W 4f XPS spectrum (Fig. 2(c)), the two peaks at the binding energies of 31.8 and 34.0 eV are the characteristic $4f_{7/2}$ and $4f_{5/2}$ peaks for metal W(0). And the two peaks located at 32.3 and 35.2 eV are featured for $4f_{7/2}$ and $4f_{5/2}$ peaks of W(IV) ions, further confirming the existence of WC phase in WC/Co_7Fe_3-NPHC. Furthermore, the two small peaks at 37.5 and 40.9 eV can be assigned to the $4f_{7/2}$ and $4f_{5/2}$ peaks of W(VI) species, which may be due to the presence of amorphous WO_x species or the coordination of W with residual oxygen-containing groups to form complexes. Besides, the spectra of C 1s (Fig. 2(d)) is fitted with four functional groups of C=C, C–P, C–N, and O–C=O, with corresponding peak values of 284.6, 285.4, 286.4, and 289.1 eV, respectively, illuminating the effective doping of N and P into carbon [43]. As exhibited in Fig. 2(e), Fe 2p spectra reveals the presence of zero-valent iron at 707.4 and 720.6 eV, while peaks at 712.5 and 726.1 eV are attributed to the $2p_{3/2}$ and $2p_{1/2}$ orbits of the Fe^{2+}/Fe^{3+} species, accompanied by satellite peaks at 716.7 and 731.1 eV [44]. Moreover, the Co 2p spectrum (Fig. 2(f)) reveals that the zero-valent cobalt is located at 778.4 and 793.9 eV, while the peaks located at 780.9 and 796.7 eV correspond to Co $2p_{3/2}$ and Co $2p_{1/2}$ of Co^{2+} species, together with the satellite peaks arising at 785.5 and 802.3 eV [45]. The above conclusions further validate the presence of Co_7Fe_3 alloys for the WC/Co_7Fe_3-NPHC. It is worth noting that compared with the Co-Fe/NC sample, the Co and Fe peaks of WC/Co_7Fe_3-NPHC shift negatively, indicating that the addition of phosphotungstic acid affects the interaction between Co and Fe and induces the modulation of electron density (Figs. S6(a) and S6(b) in the ESM). It should also be noted that Co peaks for WC/Co_7Fe_3-NPHC corresponding to the zero-valent metal are much smaller than those of Co^{2+}/Co^{3+} ionic state, and the increase of the number of Co ions with higher valence state is of great significance to improve the electrocatalytic activity [46, 47]. Two peaks appear at 129.1 and 129.9 eV in P 2p spectrum (Fig. 2(g)) and are associated with P $2p_{3/2}$ and P $2p_{1/2}$ in WC/Co_7Fe_3-NPHC. The peak of 134.2 eV can be attributed to the P–O bond, which is related to the oxidation of the substance on the surface. At the same time, we can observe the existence of P–C bond through the spectra of C 1s, and P-doping C is beneficial to improve the electron transport capacity and activity of the substrate, which has been reported in Refs. [48–50]. Figure 2(h) displays the bonding status of N in WC/Co_7Fe_3-NPHC by high-resolution N 1s spectrum, which can be deconvoluted into five peaks located at 398.6, 399.4, 400.9, 402.2, and 404.5 eV, corresponding to pyridinic-N, metal-N, pyrrolic-N, graphitic-N, and oxidized-N, respectively [51]. The percentage of nitrogen species calculated from the above fitted peaks are 28.2%, 13.1%, 35%, 14.3%, and 9.4%, respectively. Subsequently, the nitrogen configuration in WC/Co_7Fe_3-NPHC is depicted in Fig. 2(i). In general, the lone pair electrons of N heteroatoms can be used to regulate the electronic structure of carbon matrix catalysts to activate their intrinsic activity. Among the rest, the graphitic N improves the conductivity of the catalyst by providing electrons to the carbon π-conjugated system. Correspondingly, pyridinic-N can accept electrons to transfer positive charges to adjacent sp^2 hybridized carbon atoms, facilitating the adsorption of reactants, thus promoting the charge transfer between the reaction intermediates and the catalyst surface, and ultimately improving OER and ORR kinetics. In addition, the abundant pyridinic-N and pyrrolic-N also change the surface electronic properties by coordination with metal atoms, which can further improve the electrocatalytic performance.

2.2 Electrochemical activity evaluation

WC/Co_7Fe_3-NPHC is expected to be an excellent electrocatalyst for energy conversion and storage due to its porosity and heterojunction structure. Therefore, we investigated the electrocatalytic performance of WC/Co_7Fe_3-NPHC toward ORR and OER to evaluate its application potential. The ORR activity was initially assessed through cyclic voltammetry (CV) in an N_2- and O_2-saturated 0.1 M KOH solution. As can be seen from Fig. S7(a) in the ESM, there is no visible reduction peak of ORR in N_2-saturated electrolyte, while there is an obvious reduction peak (0.76 V vs. RHE) in O_2-saturated electrolyte, indicating that the material has evident activity for oxygen reduction. The reduction peak of WC/Co_7Fe_3-NPHC is more positive than those of other samples (Fig. S7(b) in the ESM), expounding that it has higher ORR activity. The ORR polarization curves of WC/Co_7Fe_3-NPHC and Pt/C catalysts in 0.1 M KOH saturated with O_2 under 1,600 rpm are displayed in Fig. 3(a). The half-wave potential ($E_{1/2}$) and limiting current density of WC/Co_7Fe_3-NPHC catalyst are 0.831 V vs. RHE and 4.740 $mA·cm^{-2}$, respectively, which are both better than Pt/C (0.829 V vs. RHE and 4.206 $mA·cm^{-2}$), and far higher than other comparison samples (Figs. S8(a) and S9(a) in the ESM). In addition, the ORR performance of WC/Co_7Fe_3-NPHC is better than that of other reported non-noble metal catalysts (Table S1 in the ESM). Therefore, it can be concluded that WC/Co_7Fe_3-NPHC has excellent ORR performance, which is put down to its large number of exposed active sites and three-dimensional structure with high specific surface area. The Tafel slope of WC/Co_7Fe_3-NPHC catalyst is 62 $mV·dec^{-1}$ (Fig. 3(b)), which is lower than Pt/C (110 $mV·dec^{-1}$) and other samples (Figs. S8(b) and S9(b) in the ESM), interpreting that WC/Co_7Fe_3-NPHC has faster ORR kinetics. Moreover, by measuring linear sweep voltammetry (LSV) curves of WC/Co_7Fe_3-NPHC at different rotational speeds by rotating disk, an approximate linear K–L curve was obtained. As shown in Fig. 3(c), the average number of transferred electrons of WC/Co_7Fe_3-NPHC catalyst is about 4.0 under a voltage range of 0.4–0.6 V, which is very close to the theoretical value of Pt/C catalyst. This result manifests that the catalyst has a direct four-electron transfer pathway to ORR and confirms the first-order kinetic process of ORR. Furthermore, the LSV curve was measured by using the rotating ring disk electrode (RRDE) technology, and the number of electron transfer (n) and the yield of hydrogen peroxide (H_2O_2) in the ORR process were calculated by the formula. As can be seen from Fig. S10(a) in the ESM, the number of electron transfer of WC/Co_7Fe_3-NPHC is in the range of 3.85–3.92 in the voltage range of 0.2–0.7 V, and the yield of H_2O_2 is below 8%, illustrating that WC/Co_7Fe_3-NPHC has four-electron selectivity like Pt/C. Impressively, the WC/Co_7Fe_3-NPHC catalyst has a minor current loss of about 6.1% after injecting 10 mL methanol, reflecting its excellent tolerance and corrosion resistance to methanol (Fig. S10(b) in the ESM). By contrast, Pt/C catalyst shows great sensitivity to methanol, resulting in a significant current loss of about 37.2%. In addition, we further calculated the electrochemical double layer capacitance (C_{dl}) from CV curves measured at different scan rates (Fig. S11 in the ESM) to reflect the proportional relationship of electrochemically active surface area (ECSA), with the WC/Co_7Fe_3-NPHC having the largest C_{dl}, which is consistent with its superior

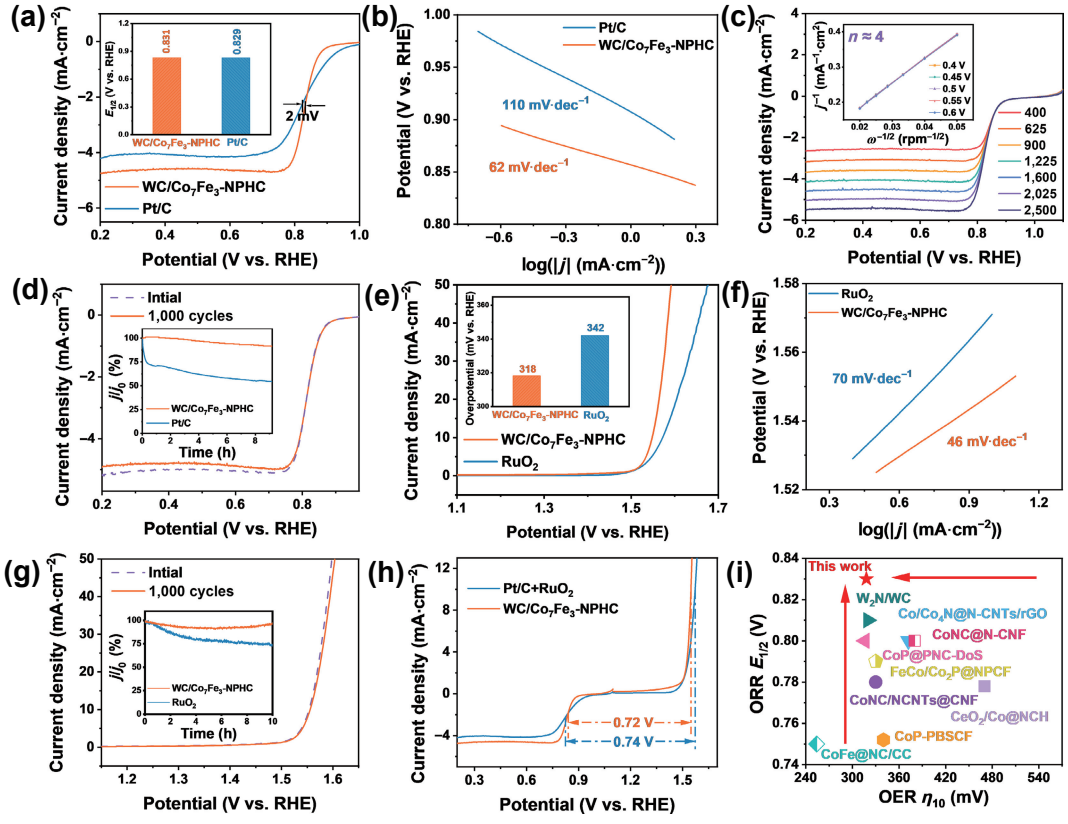

Figure 3 (a) ORR polarization curves at 1,600 rpm (inset is the bar diagram of the half-wave potential) and (b) corresponding Tafel slopes. (c) Polarization curves at different rotational speeds (inset is a fitting diagram of K–L equation at different voltages). (d) Stability of ORR. (e) OER polarization curves (inset shows the overpotential of catalysts) and (f) corresponding Tafel slopes. (g) Stability of OER. (h) The overall polarization curves within the ORR and OER and (i) bifunctional activity comparison.

ORR performance (Fig. S12 in the ESM). These results clarify that WC/Co_7Fe_3-NPHC catalyst has great ORR reaction kinetics and high selectivity for 4-electron reaction. The durability of WC/Co_7Fe_3-NPHC catalyst was tested by continuous CV firstly. The LSV curves almost overlap before and after 1,000 cycles, indicating the excellent durability of WC/Co_7Fe_3-NPHC for ORR (Fig. 3(d)), while the ORR performance of Pt/C decays significantly and with a negative half-wave potential shift of 25 mV (Fig. S13 in the ESM), indicating that the ORR stability of WC/Co_7Fe_3-NPHC is superior to that of Pt/C. Then we evaluated the long-term stability of the catalyst in 0.1 M KOH saturated with O_2 at 1,600 rpm by chronoamperometric method (inset of Fig. 3(d)). The ORR current density of WC/Co_7Fe_3-NPHC remains 91.7% of the initial value after continuous operation for 36,000 s, which is obviously stable compared with that of Pt/C. The high stability of WC/Co_7Fe_3-NPHC is attributed to its carbon shell and N,P co-doped carbon wrapped in the outer layer of the metal particles, thus preventing the metal particles from aggregation or corrosion during the electrocatalytic process. Meanwhile, the durability of WC/Co_7Fe_3-NPHC catalyst after ORR test was further clarified by SEM, XRD, and XPS. The SEM images and XRD patterns confirm that the structure of the WC/Co_7Fe_3-NPHC catalyst is well preserved and the phase remains unchanged, indicating its outstanding stability (Figs. S14(a) and S14(b) in the ESM). The XPS results illustrate that the peaks of W 4f (Fig. S15(c) in the ESM) have no significantly offset, while the peaks of Co^{2+} and Fe^{2+}/Fe^{3+} are positively shifted, which is due to the oxidation of Co and Fe to form cobalt-iron compounds with higher valence states (Figs. S15(a) and S15(b) in the ESM). Therefore, we conclude that the WC/Co_7Fe_3-NPHC catalyst holds excellent structural honesty toward ORR.

To evaluate the bifunctionality of the catalysts for rechargeable ZAB, OER performance of the catalysts was measured in 1.0 M KOH electrolyte. The overpotential of the optimized WC/Co_7Fe_3-NPHC catalyst is 318 mV at the current density of 10 $mA·cm^{-2}$, which is superior to RuO_2 (342 mV) and other catalysts (Fig. 3(e), and Figs. S16(a) and S17(a) in the ESM), demonstrating that WC/Co_7Fe_3-NPHC has excellent OER activity. The favorable reaction kinetics of WC/Co_7Fe_3-NPHC is also confirmed by the Tafel slope of 46 $mV·dec^{-1}$ in Fig. 3(f), which is smaller than RuO_2 (70 $mV·dec^{-1}$) and other control samples (Figs. S16(b) and S17(b) in the ESM). Moreover, the OER performance of WC/Co_7Fe_3-NPHC is better than that of other reported non-noble metal catalysts (Table S2 in the ESM). At the same time, we also measured the CV curves of catalysts at different scan rates (Fig. S18 in the ESM) to calculate the C_{dl} value. By comparison, it is found that WC/Co_7Fe_3-NPHC has the largest C_{dl} value, which is corresponding to its optimal OER performance (Fig. S19 in the ESM). The electrochemical impedance spectroscopy (EIS) study demonstrates that the WC/Co_7Fe_3-NPHC catalyst has a minimum charge-transfer resistance of 71.5 Ω (Fig. S20 in the ESM), verifying its fast charge transfer ability between electrode and electrolyte. In conclusion, due to the synergistic effect of Co_7Fe_3 alloy and WC heterojunction, and N,P co-doped carbon nanotubes in the catalyst, the WC/Co_7Fe_3-NPHC adsorbs and transfers more OH ions in a large extent, thus creating a rich environment for electron transfer between catalyst and electrolyte. In addition to prominent OER performance, the WC/Co_7Fe_3-NPHC also exhibits great durability, as verified by the chronoamperometric and continuous CV measurements. The LSV polarization curves of the OER remain largely unchanged after 1,000 CV cycles (Fig. 3(g)), while the catalytic activity of RuO_2 decreased significantly, with a positive overpotential shift of 20 mV at a current density 10 $mA·cm^{-2}$ (Fig. S21 in the ESM), and the current density of WC/Co_7Fe_3-NPHC kept 96.1% of the initial value after 36,000 s, which is more stable than that of RuO_2

(74.7%) (inset of Fig. 3(g)), indicating the excellent durability of WC/Co_7Fe_3-NPHC for OER. Subsequently, in order to confirm the stability of the structure and composition of the catalyst, SEM, XRD, and XPS analysis were carried out on the WC/Co_7Fe_3-NPHC after stability test. The SEM and XRD reveal that the morphology and phase of WC/Co_7Fe_3-NPHC have no obvious change after OER measurement, revealing robust stability of the catalyst (Figs. S22(a) and S22(b) in the ESM). The XPS results demonstrate that the W 4f (Fig. S23(c) in the ESM) peaks do not change significantly, and the peaks of Co^{2+} and Fe^{2+} become larger and shift slightly to the positive direction, indicating partial oxidation of Co^{2+} and Fe^{2+} (Figs. S23(a) and S23(b) in the ESM).

Overall bifunctional electrocatalytic activity for ORR and OER can be analyzed by calculating oxygen electrode activity ($\Delta E = E_{j=10} - E_{1/2}$) from the difference between OER potential at 10 $mA{\cdot}cm^{-2}$ and ORR half-wave potential, as shown in Fig. 3(h). The ΔE value of WC/Co_7Fe_3-NPHC is 0.72 V, which is smaller than that of $Pt/C+RuO_2$ (0.74 V) and also superior to the most advanced ORR and OER bifunctional catalysts (Fig. 3(i)), indicating that WC/Co_7Fe_3-NPHC has favorable reversible bifunctional activity and makes it possible to become the air cathode for ZABs.

2.3 Density functional theory (DFT) calculation

For purpose of understanding the high OER and ORR activity of the catalysts, theoretical models of WC/Co_7Fe_3/NPC (Fig. 4(a)), WC, and Co_7Fe_3 were established, and the Bader charge distribution, partial-wave state density, and d-band center of the three materials were calculated using DFT. On the grounds of the d-band center theory, the adsorption capacity for reactants is stronger as the d-band center of the material is closer to the Fermi level, which easily leads to the difficult desorption of subsequent products, resulting in the poisoning of the catalytic active site. On the contrary, the adsorption capacity is weaker as the d-band center of the material is far from the Fermi level, leading to difficulty in activating the reactants and carrying out subsequent reactions. Therefore, only when the material in a medium adsorption strength is the most conducive to the OER/ORR reaction. As can be seen from the partial-wave state density diagram of the three materials, the d-band center of WC/Co_7Fe_3/NPC structure is −0.882 eV (Fig. 4(b)) between WC cluster (−0.700 eV, Fig. 4(c)) and Co_7Fe_3 (−1.422 eV, Fig. 4(d)), inferring that WC/Co_7Fe_3/NPC structure has higher OER and ORR activity. Simultaneously, we calculated the Bader charges of Co_7Fe_3, WC clusters, and WC/Co_7Fe_3/NPC, respectively (Figs. 4(e)–4(g)). It is observed that the charge gains and losses of clusters loaded on NPC structure are more obvious than those of single clusters. The d-d orbital hybridization of Co_7Fe_3 alloy can be used to adjust the electronic structure of WC, and the polymetallic site can be used as the active center after charge redistribution to improve the atomic utilization rate and form a new reaction path. It can also be seen from the differential charge density diagram (Fig. 4(h)) that the sites near the binding of clusters and NPC become charge-enriched, which can accelerate the OER and ORR rate. In the NPC system with loaded clusters, electronic local function graph (ELF, Fig. 4(i)) is calculated to judge the bonding type and electronic local condition of clusters and carriers. It can be seen that electrons mainly appear near clusters, which is consistent with the above analysis.

2.4 Liquid and flexible Zn-air battery test

Based on the excellent OER and ORR performance of the catalyst, ZAB was assembled using WC/Co_7Fe_3-NPHC as an air electrode to evaluate its usability, and its battery performance was compared with that of the current best $Pt/C+RuO_2$ (mass ratio 1:1) catalyst [52–54]. Figure 5(a) displays a schematic diagram of ZAB. The

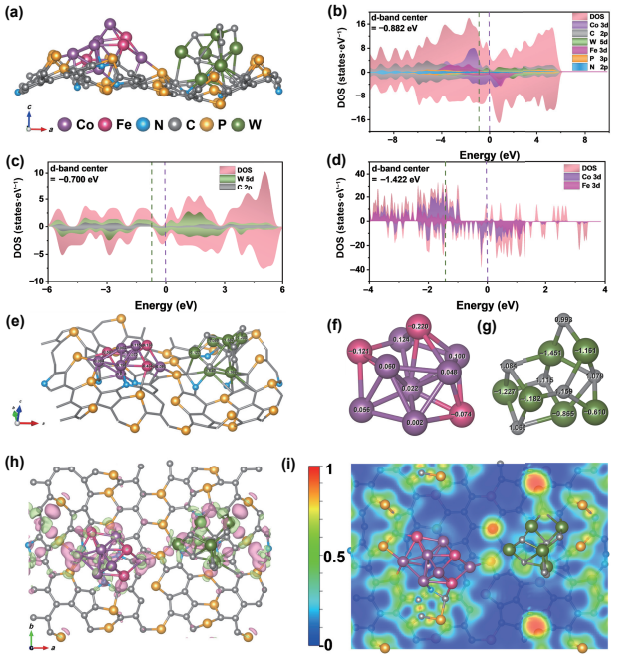

Figure 4 (a) Theoretical model of WC/Co_7Fe_3/NPC. Calculated density of states of (b) WC/Co_7Fe_3/NPC, (c) WC, and (d) Co_7Fe_3. The green and purple dashed lines represent the d-band center and Fermi level, respectively. Bader charge distribution of (e) WC/Co_7Fe_3/NPC, (f) Co_7Fe_3, and (g) WC. (h) Differential charge density and (i) ELF of WC/Co_7Fe_3/NPC.

fabricated WC/Co_7Fe_3-NPHC-based ZAB exhibits an open-circuit voltage of 1.45 V, which is slightly higher than that of the $Pt/C+RuO_2$ battery (1.43 V, Fig. 5(b)). And Fig. 5(c) is the charge and discharge polarization curves, revealing that WC/Co_7Fe_3-NPHC-based ZAB has a very small voltage gap of 0.72 V at a current density of 100 $mA{\cdot}cm^{-2}$, lower than that of $Pt/C+RuO_2$-based ZAB (0.77 V), clarifying its remarkable energy conversion efficiency. According to the discharge curve, the WC/Co_7Fe_3-NPHC-based battery delivers a peak power density of 270 $mW{\cdot}cm^{-2}$ at 489 $mA{\cdot}cm^{-2}$ (Fig. 5(d)), which is higher than that of $Pt/C+RuO_2$-based battery (196 $mW{\cdot}cm^{-2}$) and other reported non-noble-metal-based ZABs (Table S3 in the ESM). Moreover, with the increase of current density, the change of discharge voltage of WC/Co_7Fe_3-NPHC-based ZAB is less than that of $Pt/C+RuO_2$, and when the current density is restored to the initial value, the discharge voltage of WC/Co_7Fe_3-NPHC-based ZAB can also be restored to the original level, indicating its brilliant discharge performance and reversibility (Fig. 5(e)). Correspondingly, as shown in Fig. S24 in the ESM, the specific discharge capacity of WC/Co_7Fe_3-NPHC-based ZAB is determined to be 928.9, 870.5, and 818.8 $mAh{\cdot}g^{-1}$ (when normalized to the mass of the consumed Zn anode) at 5, 10, and 20 $mA{\cdot}cm^{-2}$, respectively. In Fig. 5(f), a long-time charge and discharge cycle test was conducted at a current density of 10 $mA{\cdot}cm^{-2}$ to certify the durability of batteries. It can be seen that after 550 h of continuous operation, the WC/Co_7Fe_3-NPHC-based ZAB still remains a small voltage gap (0.59 V), and the round-trip efficiency remains at 67.0%. While the battery of $Pt/C+RuO_2$ can only run continuously for 130 h with the voltage gap of 1.28 V and keep a round-trip efficiency of 46.4%. These results further prove that WC/Co_7Fe_3-NPHC-based ZAB has better durability and higher reversible energy conversion efficiency than $Pt/C+RuO_2$ ZAB. Therefore, the unique hierarchical structure and abundant active sites endow WC/Co_7Fe_3-NPHC a promising electrocatalytic material to realize high-power and long-life Zn-air batteries.

In light of excellent performance of WC/Co_7Fe_3-NPHC-based ZABs, we further assembled flexible solid-state Zn-air batteries

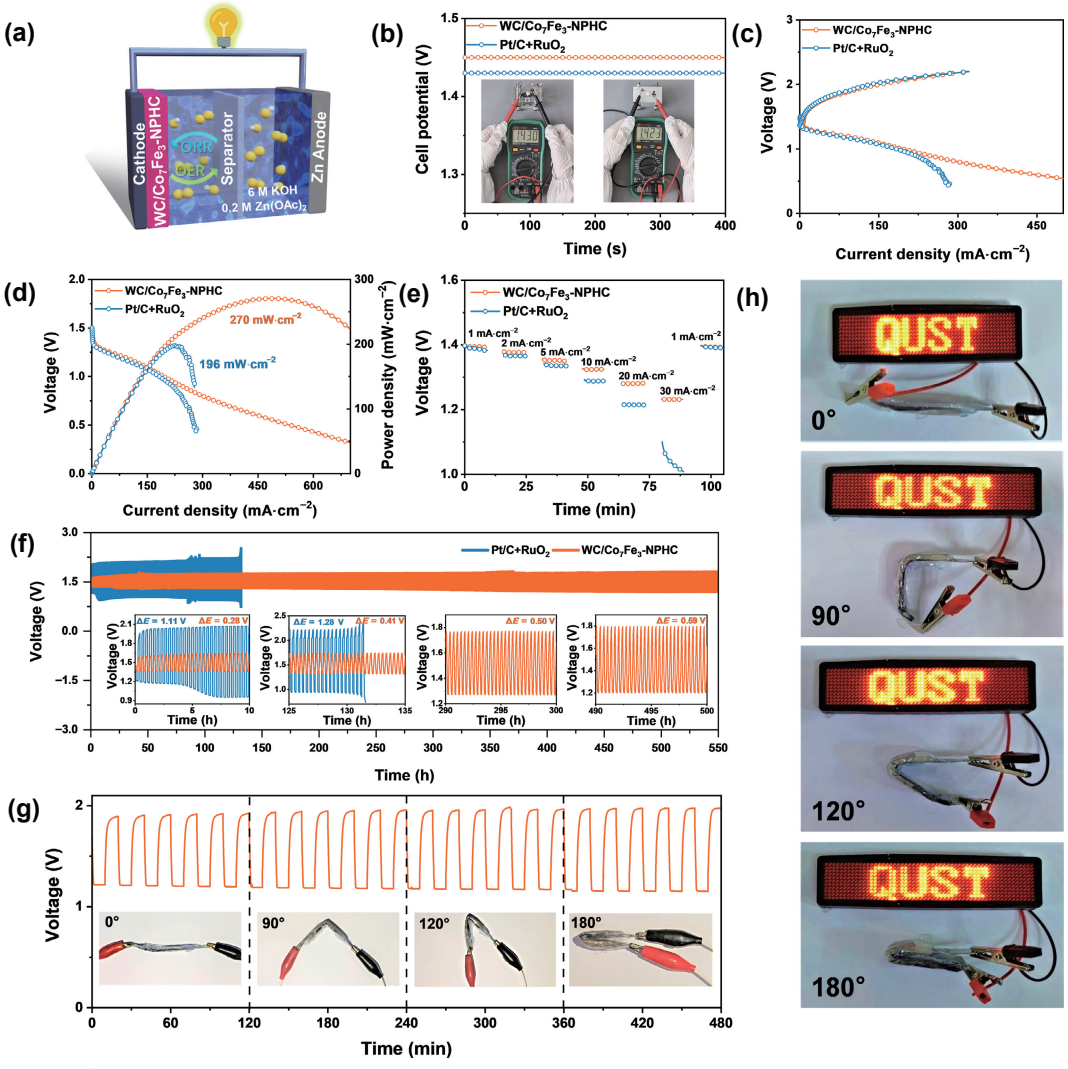

Figure 5 (a) Schematic of ZAB. (b) Open circuit voltage, (c) charge and discharge polarization curves, (d) discharge polarization curves and related power density curves, (e) discharge curves at different current densities, and (f) galvanostatic charge–discharge cycling stability of liquid ZAB. (g) Cycling test in mimicking real bending circumstances of flexible ZAB. (h) Photos of LEDs powered by flexible ZAB at different bending angles.

assembled with an air electrode (WC/Co_7Fe_3-NPHC loaded on waterproof and breathable film), an alkaline gel polymer electrolyte, and a Zn foil [55–57]. The WC/Co_7Fe_3-NPHC-based ZAB is tested in mimicking real bending circumstances, as demonstrated in Fig. 5(g). Amazingly, the sandwich-type ZAB keep delivering unimpaired voltage profiles when we bent it from 0° to 180°, and its voltage gap and round-trip efficiency have no significant change (0.72 V-62.5% at 0°, 0.77 V-60.4% at 90°, 0.79 V-59.6% at 120°, and 0.82 V-58.4% at 180°, respectively), reflecting its enhanced flexibility and mechanical durability. Figure 5(h) further proves that the flexible battery can light up the light-emitting diode (LED) lamp at different bending angles, indicating the application potential of the WC/Co_7Fe_3-NPHC catalyst. The above results demonstrate that WC/Co_7Fe_3-NPHC-based ZAB has strong competitiveness in practical application due to its durability and bending resistance.

3 Conclusions

In summary, we elaborately synthesized WC/Co_7Fe_3-NPHC heterostructure through simple chemical precipitation and pyrolysis strategy. Profiting by the synergistic effect among the WC, Co_7Fe_3, and N,P co-doped carbon at the three-phase heterojunction interface, as well as the distinct hierarchical carbon structure, the WC/Co_7Fe_3-NPHC has excellent OER (η_{10} = 318 mV) and ORR ($E_{1/2}$ = 0.831 V vs. RHE) activities. Theoretical calculation further confirms the mutual adjustment between the WC and Co_7Fe_3 and N,P co-doped carbon and makes the catalyst have moderate adsorption strength, and greatly improves the conductivity and electron transfer rate of the material. When applied to liquid ZAB, the WC/Co_7Fe_3-NPHC electrode shows a narrow charge–discharge gap and maintains a large degree of stable activity even after 550 h. When applied to flexible solid ZAB, the battery can keep good charge and discharge stability at different bending angles. This work provides a novel approach to the design of heterostructure catalysts, and provides a new strategy for the development of Zn-air batteries with high performance, power/energy density, and durability.

Acknowledgements

This work was financially supported from the National Natural Science Foundation of China (Nos. 51772162 and 52072197), China Postdoctoral Science Foundation (No. 2020M682135), Postdoctoral Applied Research Project of Qingdao, Postdoctoral Innovation Project of Shandong Province (No. 202102039), Outstanding Youth Foundation of Shandong Province, China (No. ZR2019JQ14), Youth Innovation and Technology Foundation of Shandong Higher Education Institutions, China (No. 2019KJC004), the Natural Science Foundation of Shandong Province (No. ZR2021MB085), Major Scientific and Technological Innovation Project (No. 2019JZZY020405), Major

Basic Research Program of Natural Science Foundation of Shandong Province under Grant (No. ZR2020ZD09), and Taishan Scholar Young Talent Program (No. tsqn201909114).

Electronic Supplementary Material: Supplementary material (the Experimental section; SEM images of different precursors; SEM images, XRD patterns, Raman and XPS spectra of various catalysts; CV curves; ORR and OER polarization curves and Tafel plots; peroxide production and electron transfer number; methanol tolerance for ORR; properties of Pt/C and RuO_2 after 1,000 CV cycles; SEM images, XRD patterns and XPS spectra after OER and ORR; EIS; specific capacities of ZABs; and performance comparison table) is available in the online version of this article at https://doi.org/10.1007/s12274-022-5059-y.

References

[1] Gao, D. F.; Li, H. F.; Wei, P. F.; Wang, Y.; Wang, G. X.; Bao, X. H. Electrochemical synthesis of catalytic materials for energy catalysis. *Chin. J. Catal.* **2022**, *43*, 1001–1016.

[2] Goodenough, J. B. Electrochemical energy storage in a sustainable modern society. *Energy Environ. Sci.* **2014**, *7*, 14–18.

[3] Guo, Y. B.; Chen, Y. N.; Cui, H. J.; Zhou, Z. Bifunctional electrocatalysts for rechargeable Zn-air batteries. *Chin. J. Catal.* **2019**, *40*, 1298–1310.

[4] Wu, M. J.; Zhang, G. X.; Wu, M. H.; Prakash, J.; Sun, S. H. Rational design of multifunctional air electrodes for rechargeable Zn-air batteries: Recent progress and future perspectives. *Energy Stor. Mater.* **2019**, *21*, 253–286.

[5] Zhu, B. J.; Liang, Z. B.; Xia, D. G.; Zou, R. Q. Metal-organic frameworks and their derivatives for metal-air batteries. *Energy Stor. Mater.* **2019**, *23*, 757–771.

[6] Wu, Z. H.; Yu, Y. R.; Zhang, G. K.; Zhang, Y. S.; Guo, R. X.; Li, L.; Zhao, Y. G.; Wang, Z.; Shen, Y. L.; Shao, G. S. *In situ* monitored (N,O)-doping of flexible vertical graphene films with high-flux plasma enhanced chemical vapor deposition for remarkable metal-free redox catalysis essential to alkaline zinc-air batteries. *Adv. Sci.* **2022**, *9*, 2200614.

[7] Lei, H.; Yang, S. J.; Wan, Q. X.; Ma, L.; Javed, M. S.; Tan, S. Z.; Wang, Z. L.; Mai, W. Coordination and interface engineering to boost catalytic property of two-dimensional ZIFs for wearable Zn-air batteries. *J. Energy Chem.* **2022**, *68*, 78–86.

[8] Chen, D. F.; Pan, L.; Pei, P. C.; Song, X.; Ren, P.; Zhang, L. Cobalt-based oxygen electrocatalysts for zinc-air batteries: Recent progress, challenges, and perspectives. *Nano Res.* **2022**, *15*, 5038–5063.

[9] Zhang, Z. Y.; Tan, Y. Y.; Zeng, T.; Yu, L. Y.; Chen, R.; Cheng, N. C.; Mu, S. C.; Sun, X. L. Tuning the dual-active sites of ZIF-67 derived porous nanomaterials for boosting oxygen catalysis and rechargeable Zn-air batteries. *Nano Res.* **2020**, *14*, 2353–2362.

[10] Li, Y. J.; Sun, Y. J.; Qin, Y. N.; Zhang, W. Y.; Wang, L.; Luo, M. C.; Yang, H.; Guo, S. J. Recent advances on water-splitting electrocatalysis mediated by noble-metal-based nanostructured materials. *Adv. Energy Mater.* **2020**, *10*, 1903120.

[11] Kwon, T.; Kim, T.; Son, Y.; Lee, K. Dopants in the design of noble metal nanoparticle electrocatalysts and their effect on surface energy and coordination chemistry at the nanocrystal surface. *Adv. Energy Mater.* **2021**, *11*, 2100265.

[12] Wang, C.; Van Der Vliet, D.; More, K. L.; Zaluzec, N. J.; Peng, S.; Sun, S. H.; Daimon, H.; Wang, G. F.; Greeley, J.; Pearson, J. et al. Multimetallic Au/$FePt_3$ nanoparticles as highly durable electrocatalyst. *Nano Lett.* **2011**, *11*, 919–926.

[13] Spöri, C.; Briois, P.; Nong, H. N.; Reier, T.; Billard, A.; Kühl, S.; Teschner, D.; Strasser, P. Experimental activity descriptors for iridium-based catalysts for the electrochemical oxygen evolution reaction (OER). *ACS Catal.* **2019**, *9*, 6653–6663.

[14] Hu, C. L.; Zhang, L.; Gong, J. L. Recent progress made in the mechanism comprehension and design of electrocatalysts for alkaline water splitting. *Energy Environ. Sci.* **2019**, *12*, 2620–2645.

[15] Ghosh, S.; Basu, R. N. Multifunctional nanostructured electrocatalysts for energy conversion and storage: Current status and perspectives. *Nanoscale* **2018**, *10*, 11241–11280.

[16] Chen, Y. P.; Lin, S. Y.; Sun, R. M.; Wang, A. J.; Zhang, L.; Ma, X. H.; Feng, J. J. FeCo/FeCoP encapsulated in N,Mn-codoped three-dimensional fluffy porous carbon nanostructures as highly efficient bifunctional electrocatalyst with multi-components synergistic catalysis for ultra-stable rechargeable Zn-air batteries. *J. Colloid Interface Sci.* **2022**, *605*, 451–462.

[17] Hu, C. G.; Dai, L. M. Multifunctional carbon-based metal-free electrocatalysts for simultaneous oxygen reduction, oxygen evolution, and hydrogen evolution. *Adv. Mater.* **2017**, *29*, 1604942.

[18] Hou, C. C.; Zou, L. L.; Wang, Y.; Xu, Q. MOF-mediated fabrication of a porous 3D superstructure of carbon nanosheets decorated with ultrafine cobalt phosphide nanoparticles for efficient electrocatalysis and zinc-air batteries. *Angew. Chem., Int. Ed.* **2020**, *59*, 21360–21366.

[19] Han, X. P.; Ling, X. F.; Wang, Y.; Ma, T. Y.; Zhong, C.; Hu, W. B.; Deng, Y. D. Generation of nanoparticle, atomic-cluster, and single-atom cobalt catalysts from zeolitic imidazole frameworks by spatial isolation and their use in zinc-air batteries. *Angew. Chem., Int. Ed.* **2019**, *58*, 5359–5364.

[20] Li, Y. B.; Tan, X.; Tan, H.; Ren, H. J.; Chen, S.; Yang, W. F.; Smith, S. C.; Zhao, C. Phosphine vapor-assisted construction of heterostructured $Ni_2P/NiTe_2$ catalysts for efficient hydrogen evolution. *Energy Environ. Sci.* **2020**, *13*, 1799–1807.

[21] Bai, J. M.; Meng, T.; Guo, D. L.; Wang, S. G.; Mao, B. G.; Cao, M. H. Co_9S_8@MoS_2 core–shell heterostructures as trifunctional electrocatalysts for overall water splitting and Zn-air batteries. *ACS Appl. Mater. Interfaces* **2018**, *10*, 1678–1689.

[22] Qian, Q. Z.; Li, Y. P.; Liu, Y.; Guo, Y. M.; Li, Z. Y.; Zhu, Y.; Zhang, G. Q. Hierarchical multi-component nanosheet array electrode with abundant NiCo/$MoNi_4$ heterostructure interfaces enables superior bifunctionality towards hydrazine oxidation assisted energy-saving hydrogen generation. *Chem. Eng. J.* **2021**, *414*, 128818.

[23] Diao, J. X.; Qiu, Y.; Liu, S. Q.; Wang, W. T.; Chen, K.; Li, H. L.; Yuan, W. Y.; Qu, Y. T.; Guo, X. H. Interfacial engineering of W_2N/WC heterostructures derived from solid-state synthesis: A highly efficient trifunctional electrocatalyst for ORR, OER, and HER. *Adv. Mater.* **2020**, *32*, 1905679.

[24] Regmi, Y. N.; Waetzig, G. R.; Duffee, K. D.; Schmuecker, S. M.; Thode, J. M.; Leonard, B. M. Carbides of group IVA, VA and VIA transition metals as alternative HER and ORR catalysts and support materials. *J. Mater. Chem. A* **2015**, *3*, 10085–10091.

[25] Song, L. H.; Zhang, J.; Sarkar, S.; Zhao, C. F.; Wang, Z. W.; Huang, C. Y.; Yan, L. M.; Zhao, Y. F. Interface engineering of FeCo-Co structure as bifunctional oxygen electrocatalyst for rechargeable zinc-air batteries via alloying degree control strategy. *Chem. Eng. J.* **2022**, *433*, 133686.

[26] Samanta, A.; Raj, C. R. Catalyst support in oxygen electrocatalysis: A case study with CoFe alloy electrocatalyst. *J. Phys. Chem. C* **2018**, *122*, 15843–15852.

[27] Su, W.; Yan, P. P.; Wei, X. F.; Zhu, X. W.; Zhou, Q. Y. Facile one-step synthesis of nitrogen-doped carbon sheets supported tungsten carbide nanoparticles electrocatalyst for hydrogen evolution reaction. *Int. J. Hydrogen Energy* **2020**, *45*, 33430–33439.

[28] Xu, L.; Wu, S. Q.; Deng, D. J.; Wang, C.; Qian, J. C.; Lu, G. F.; Li, H. N. Fabricating highly active and stable tungsten carbide electrocatalyst for rechargeable zinc-air batteries: An approach of dual metal Co-adjusted the electronic structure. *J. Alloys Compd.* **2021**, *868*, 159236.

[29] Zhu, H.; Sun, Z. N.; Chen, M. L.; Cao, H. H.; Li, K.; Cai, Y. Z.; Wang, F. H. Highly porous composite based on tungsten carbide and N-doped carbon aerogels for electrocatalyzing oxygen reduction reaction in acidic and alkaline media. *Electrochim. Acta* **2017**, *236*, 154–160.

[30] Lei, Z.; Tan, Y. Y.; Zhang, Z. Y.; Wu, W.; Cheng, N. C.; Chen, R. Z.; Mu, S. C.; Sun, X. L. Defects enriched hollow porous Co-N-doped carbons embedded with ultrafine CoFe/Co nanoparticles as bifunctional oxygen electrocatalyst for rechargeable flexible solid

zinc-air batteries. *Nano Res.* **2021**, *14*, 868–878.
[31] Xiong, X.; Jiang, R.; Deng, B. W.; Yang, J.; Wang, D. H. Bionic structural design and electrochemical manufacture of WC/N-doped carbon hybrids as efficient ORR catalyst. *J. Electrochem. Soc.* **2020**, *167*, 064502.
[32] Liu, T. T.; Li, M.; Bo, X. J.; Zhou, M. Designing transition metal alloy nanoparticles embedded hierarchically porous carbon nanosheets as high-efficiency electrocatalysts toward full water splitting. *J. Colloid Interface Sci.* **2019**, *537*, 280–294.
[33] Wang, Y. Y.; Kumar, A.; Ma, M.; Jia, Y.; Wang, Y.; Zhang, Y.; Zhang, G. X.; Sun, X. M.; Yan, Z. F. Hierarchical peony-like FeCo-NC with conductive network and highly active sites as efficient electrocatalyst for rechargeable Zn-air battery. *Nano Res.* **2020**, *13*, 1090–1099.
[34] Riyajuddin, S.; Azmi, K.; Pahuja, M.; Kumar, S.; Maruyama, T.; Bera, C.; Ghosh, K. Super-hydrophilic hierarchical Ni-foam-graphene-carbon nanotubes-Ni_2P-CuP_2 nano-architecture as efficient electrocatalyst for overall water splitting. *ACS Nano* **2021**, *15*, 5586–5599.
[35] Xu, Z. X.; Zhuang, X. D.; Yang, C. Q.; Cao, J.; Yao, Z. Q.; Tang, Y. P.; Jiang, J. Z.; Wu, D. Q.; Feng, X. L. Nitrogen-doped porous carbon superstructures derived from hierarchical assembly of polyimide nanosheets. *Adv. Mater.* **2016**, *28*, 1981–1987.
[36] Xie, W. F.; Li, J. M.; Song, Y. K.; Li, S. J.; Li, J. B.; Shao, M. F. Hierarchical carbon microtube@nanotube core–shell structure for high-performance oxygen electrocatalysis and Zn-air battery. *Nano-Micro Lett.* **2020**, *12*, 97.
[37] Wang, Y. N.; Zhou, J.; He, Y.; Liu, Y. F.; Xu, C. L. Highly performed nitrogen-doped porous carbon electrocatalyst for oxygen reduction reaction prepared by a simple and slight regulation in hydrolyzing process of ZIF-8. *J. Solid State Chem.* **2021**, *302*, 122415.
[38] Lu, X. F.; Fang, Y. J.; Luan, D. Y.; Lou, X. W. D. Metal-organic frameworks derived functional materials for electrochemical energy storage and conversion: A mini review. *Nano Lett.* **2021**, *21*, 1555–1565.
[39] Zhao, X. H.; Pattengale, B.; Fan, D. H.; Zou, Z. H.; Zhao, Y. Q.; Du, J.; Huang, J. F.; Xu, C. L. Mixed-node metal-organic frameworks as efficient electrocatalysts for oxygen evolution reaction. *ACS Energy Lett.* **2018**, *3*, 2520–2526.
[40] Qiu, T. J.; Liang, Z. B.; Guo, W. H.; Tabassum, H.; Gao, S.; Zou, R. Q. Metal-organic framework-based materials for energy conversion and storage. *ACS Energy Lett.* **2020**, *5*, 520–532.
[41] Zhao, C. X.; Liu, J. N.; Wang, J.; Wang, C. D.; Guo, X.; Li, X. Y.; Chen, X.; Song, L.; Li, B. Q.; Zhang, Q. A clicking confinement strategy to fabricate transition metal single-atom sites for bifunctional oxygen electrocatalysis. *Sci. Adv.* **2022**, *8*, eabn5091.
[42] Balamurugan, J.; Nguyen, T. T.; Kim, D. H.; Kim, N. H.; Lee, J. H. 3D nickel molybdenum oxyselenide ($Ni_{1-x}Mo_xOSe$) nanoarchitectures as advanced multifunctional catalyst for Zn-air batteries and water splitting. *Appl. Catal. B:Environ.* **2021**, *286*, 119909.
[43] Qin, Q.; Jang, H.; Chen, L. L.; Nam, G.; Liu, X. E.; Cho, J. Low loading of Rh_xP and RuP on N, P codoped carbon as two trifunctional electrocatalysts for the oxygen and hydrogen electrode reactions. *Adv. Energy Mater.* **2018**, *8*, 1801478.
[44] Chen, X.; Pu, J.; Hu, X. H.; An, L.; Jiang, J. J.; Li, Y. J. Confinement synthesis of bimetallic MOF-derived defect-rich nanofiber electrocatalysts for rechargeable Zn-air battery. *Nano Res.* , in press,https://doi.org/10.1007/s12274-022-4563-4.
[45] Lu, X. F.; Chen, Y.; Wang, S. B.; Gao, S. Y.; Lou, X. W. Interfacing manganese oxide and cobalt in porous graphitic carbon polyhedrons boosts oxygen electrocatalysis for Zn-air batteries. *Adv. Mater.* **2019**, *31*, 1902339.
[46] Liu, Z. Q.; Cheng, H.; Li, N.; Ma, T. Y.; Su, Y. Z. $ZnCo_2O_4$ quantum dots anchored on nitrogen-doped carbon nanotubes as reversible oxygen reduction/evolution electrocatalysts. *Adv. Mater.* **2016**, *28*, 3777–3784.
[47] Yu, J. H.; Cui, Z. X.; Li, X.; Chen, D.; Ji, J. W.; Zhang, Q.; Sui, J.; Yu, L. Y.; Dong, L. F. Facile fabrication of ZIF-derived graphene-based 2D Zn/Co oxide hybrid for high-performance supercapacitors. *J. Energy Storage* **2020**, *27*, 101165.
[48] Zhang, J.; Shi, Y.; Ding, Y.; Peng, L. L.; Zhang, W. K.; Yu, G. H. A conductive molecular framework derived Li_2S/N,P-codoped carbon cathode for advanced lithium-sulfur batteries. *Adv. Energy Mater.* **2017**, *7*, 1602876.
[49] Zheng, Y.; Jiao, Y.; Li, L. H.; Xing, T.; Chen, Y.; Jaroniec, M.; Qiao, S. Z. Toward design of synergistically active carbon-based catalysts for electrocatalytic hydrogen evolution. *ACS Nano* **2014**, *8*, 5290–5296.
[50] Wang, Q. T.; Cui, K.; Li, J.; Wu, Y. X.; Yang, Y. X.; Zhou, X. Z.; Ma, G. F.; Yang, Z. W.; Lei, Z. Q.; Ren, S. F. Phosphorus-doped $CoTe_2$/C nanoparticles create new Co-P active sites to promote the hydrogen evolution reaction. *Nanoscale* **2020**, *12*, 9171–9177.
[51] Xu, Q. C.; Jiang, H.; Li, Y. H.; Liang, D.; Hu, Y. J.; Li, C. Z. *In-situ* enriching active sites on co-doped Fe-Co_4N@N-C nanosheet array as air cathode for flexible rechargeable Zn-air batteries. *Appl. Catal. B: Environ.* **2019**, *256*, 117893.
[52] Zhang, M.; Zhang, J. T.; Ran, S. Y.; Qiu, L. X.; Sun, W.; Yu, Y.; Chen, J. S.; Zhu, Z. H. A robust bifunctional catalyst for rechargeable Zn-air batteries: Ultrathin NiFe-LDH nanowalls vertically anchored on soybean-derived Fe-N-C matrix. *Nano Res.* **2021**, *14*, 1175–1186.
[53] Lu, X. F.; Zhang, S. L.; Shangguan, E. B.; Zhang, P.; Gao, S. Y.; Lou, X. W. Nitrogen-doped cobalt pyrite yolk–shell hollow spheres for long-life rechargeable Zn-air batteries. *Adv. Sci.* **2020**, *7*, 2001178.
[54] Zhou, C. H.; Chen, X.; Liu, S.; Han, Y.; Meng, H. B.; Jiang, Q. Y.; Zhao, S. M.; Wei, F.; Sun, J.; Tan, T. et al. Superdurable bifunctional oxygen electrocatalyst for high-performance zinc-air batteries. *J. Am. Chem. Soc.* **2022**, *144*, 2694–2704.
[55] He, Y. T.; Yang, X. X.; Li, Y. S.; Liu, L. T.; Guo, S. W.; Shu, C. Y.; Liu, F.; Liu, Y. N.; Tan, Q.; Wu, G. Atomically dispersed Fe-Co dual metal sites as bifunctional oxygen electrocatalysts for rechargeable and flexible Zn-air batteries. *ACS Catal.* **2022**, *12*, 1216–1227.
[56] Qiang, F. Q.; Feng, J. G.; Wang, H. L.; Yu, J. H.; Shi, J.; Huang, M. H.; Shi, Z. C.; Liu, S.; Li, P.; Dong, L. F. Oxygen engineering enables N-doped porous carbon nanofibers as oxygen reduction/evolution reaction electrocatalysts for flexible zinc-air batteries. *ACS Catal.* **2022**, *12*, 4002–4015.
[57] Wagh, N. K.; Kim, D. H.; Kim, S. H.; Shinde, S. S.; Lee, J. H. Heuristic iron-cobalt-mediated robust pH-universal oxygen bifunctional lusters for reversible aqueous and flexible solid-state Zn-air cells. *ACS Nano* **2021**, *15*, 14683–14696.